ADVANCED ENERGY & SUSTAINABILITY RESEARCH
www.advenergysustres.com

Understanding and Tuning Fe-Doping on Zn–Fe Layered Double Hydroxide Particle and Photocatalytic Properties

Shaoqing Qu, Ruiman Ma, Igor Efimov, Eftychios Hadjittofis, Sergio Vernuccio, and Kyra Sedransk Campbell**

Zn-based layered double hydroxides (LDHs) are promising photocatalytic materials, but their synthesis faces environmental and economic challenges. Oxidative ionothermal synthesis (OIS) offers a green route for zinc oxide synthesis using ionic liquids. To reduce costs, the OIS method uses recovered zinc-containing mixed metal systems, such as electric arc furnace dust, instead of pure metallic Zn. Understanding the interaction of Zn with impure metals during oxidation is essential. This study employs 1-Butyl-3-methylimidazolium chloride ([BMIM]Cl) as the solvent and Fe-doped metallic Zn, the most common waste-stream metal, as the starting material. This study applies quartz crystal microbalance with dissipation to monitor product formation, and X-ray diffraction and scanning electron microscopy to characterize composition and morphology. Results show that $FeCl_2$ doping accelerates the reaction, transforming simonkolleite to Zn–Fe LDH with tunable morphologies. A reaction mechanism for Zn in [BMIM]Cl with $FeCl_2$ is proposed. Photocatalytic hydrogen production tests reveal a favorable hydrogen evolution rate of 20.9 $\mu mol\ h^{-1}\ g^{-1}$ with 0.45 M $FeCl_2$ doping, attributed to improved surface structure and crystallinity of the hydrotalcite.

1. Introduction

Nanoparticles (NPs) of Zn-based layered double hydroxides (LDH) have a distinctive structure consisting of Zn-OH octahedral framework layers, with some of the Zn^{2+} ions being replaced by trivalent metal ions, alternatingly stacked with anionic layers.[1] This unique crystal structure imparts various applications to Zn-based LDH, including biomedical applications,[2] degradation,[3] and photocatalysis.[4] In particular, Zn-based LDHs show potential for photocatalytic hydrogen production, providing a sustainable method for harnessing solar energy.[5] Their unique structure and wide tunability make them cost-effective alternatives to ZnO-based materials.[5–8] Metal doping in LDHs has proven to be an effective strategy to enhance photocatalytic performance, garnering significant attention from researchers.[9,10] However, the morphology of Zn-based LDH is a critical factor influencing their photocatalytic performance.[11] Parida et al. and Zazoua et al. discussed the influence of iron on the photocatalytic performance of LDH. The results showed that excess Fe^{3+} dopant led to the formation of amorphous iron oxide and negatively affected the reaction rate, highlighting the importance of controlling the material's morphology to optimize catalytic performance.[11,12] However, synthesizing high-purity LDH with controlled morphology is not straightforward. The most common synthesis method is coprecipitation,[1] which involves mixing a Zn salt with another metal salt in a specific ratio in an aqueous solution, followed by pH adjustment.[13,14] This method typically requires soluble salt with the base, potentially polluting the environment. Some other methods, such as hydrothermal[15] and homogeneous precipitation,[16] are also constrained by similar factors, including environmental concerns, complex operation, and energy consumption.

Malaret et al. synthesized controllable ZnO morphologies by oxidative ionothermal synthesis (OIS),[17] utilizing the aqueous solution of an ionic liquid (IL), 1-Butyl-3-methylimidazolium chloride ([BMIM]Cl), as a solvent to produce ZnO with its derivatives from metallic Zn. [BMIM]Cl is an imidazolium IL (**Figure 1**a) containing a hydrophilic imidazole ring with a hydrophobic alkyl chain. The molecular structure of the surfactants enables the self-assembly of [BMIM]Cl, which can be utilized to synthesize NPs with controllable morphologies.[18–20] Likewise, owing to extremely low volatility, stability, and recyclability, imidazolium ILs have become favored green solvents.[21] The method proposed by Malaret et al. offers an environmentally friendly approach to produce ZnO NPs with controllable morphologies, such as nanospheres, nanosheets, and nanorods, by simply adjusting the concentration of [BMIM]Cl and the reaction temperature. However, this method requires long reaction times

S. Qu, R. Ma, I. Efimov, E. Hadjittofis, S. Vernuccio, K. S. Campbell
School of Chemical, Materials and Biological Engineering
University of Sheffield
Sheffield S1 4LZ, UK
E-mail: s.vernuccio@sheffield.ac.uk; k.sedransk@sheffield.ac.uk

S. Vernuccio
School of Chemistry and Chemical Engineering
University of Southampton
Southampton SO17 1BJ, UK

The ORCID identification number(s) for the author(s) of this article can be found under https://doi.org/10.1002/aesr.202400309.

DOI: 10.1002/aesr.202400309

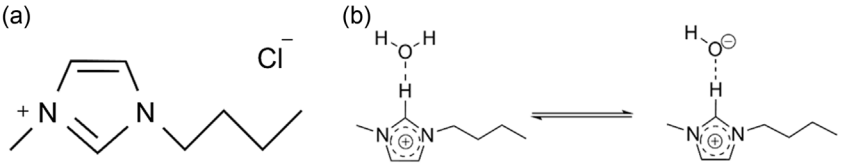

Figure 1. a) The chemical structure of [BMIM]Cl; b) $[BMIM]^+$ deprotonation with its Lewis base pairs.

(4–15 days), limiting its practicality for industrial applications. Additionally, using high-purity metallic zinc as the zinc source restricts the method's broader applicability and cost-effectiveness.

Our previous study successfully applied the OIS method, using Betaine hydrochloride, to produce high-purity morphology-controllable simonkolleite nanosheets.[22] This method significantly reduces the reaction time to 24 h to synthesize high-purity microscale particles. The resulting simonkolleite particles exhibit hexagonal sheets and possess a layered crystal structure similar to that of LDH. However, several challenges related to the use of Betaine hydrochloride remain to be addressed. Using pure Zn grains as the source material has high costs for industrial production, limiting its direct application. On the contrary, the OIS method was initially designed specifically for the cost-effective and environmentally friendly utilization of recovered zinc, such as waste galvanized steel[23] and electric arc furnace dust.[24] Synthesis starting from the waste stream holds distinct advantages compared to conventional hydrothermal synthesis and coprecipitation methods.[17,25,26] However, introducing impurity ions leads to significant changes in the morphology of the synthesized Zn-based nanosheets.[27,28] Hence, understanding the interaction between Zn and impure metal in ILs is imperative for an effective industrial application of the OIS method.

This study proposes the use of [BMIM]Cl IL with metallic zinc to synthesize Zn-based LDH through the OIS method at room temperature. The work focuses on the oxidation behavior of metallic zinc in the presence of Fe ions —the most common metal associated with zinc— in the IL. Quartz crystal microbalance with dissipation (QCMD) was used to investigate the formation and growth kinetics of Zn-based LDH. The products were characterized using X-ray diffraction (XRD), scanning electron microscopy (SEM), and energy dispersive X-ray spectroscopy (EDX). Based on the results of the characterizations, a growth mechanism for Zn in [BMIM]Cl was proposed. Finally, the synthesized Zn-based material was tested as a photocatalyst for hydrogen production, using methanol as a sacrificial agent, to demonstrate the potential of Zn-based LDH in photocatalysis.

2. Results and Discussion

2.1. Compositional Analysis

All samples exhibited a noticeable change after the 24 h reaction period, with the initially clear liquid phase gradually becoming clouded as the reaction progressed. In the absence of iron, the liquid displayed a white suspension. Conversely, in the presence of iron doping, the suspension exhibited a yellow color, with the intensity increasing as the iron concentration was raised. This behavior is consistent with findings from previous research.[29] To further investigate the effect of iron concentration on the particle formation process, phase analysis was initially carried out using XRD.

2.1.1. Noniron Doping Groups

The categories involving $ZnCl_2$-doping and NaCl-doping are regarded as noniron doping groups. In these cases, the resulting product appears as a fine white powder that separates from the suspension.

The XRD patterns of $ZnCl_2$ doping cases reveal that the predominant composition of the material is simonkolleite (**Figure 2**b). In case of high concentration, particularly with Zn doping reaching 0.54 M, the specific peak [003] at 11.2° becomes prominent and sharp, while low-intensity additional peaks are observed. This indicates the crystallization of simonkolleite with high purity. As the concentration of $ZnCl_2$ decreases, the intensity of simonkolleite weakens, and a shift in the [003] signal is evident in the 0.18 M $ZnCl_2$-doped case. Additionally, the characteristic peaks of simonkolleite, including [202] and its adjacent peaks, disappear. The diffraction pattern between 32° to 42° is more consistent with zinc hydroxide than with simonkolleite. The nondoped cases are characterized by significant peaks of ϵ-$Zn(OH)_2$ at 20.2°, 20.9°, 27.2°, and 27.8°, corresponding to the crystal planes [011], [101], [111], and [102], respectively. Additionally, only a few minor impurity peaks are detected, suggesting that the main components of the product in the nondoped case are zinc hydroxide and Zn oxide.

The XRD patterns of the $ZnCl_2$-doping cases indicate that the formation of simonkolleite is strongly related to the $ZnCl_2$ concentration. Metallic Zn is oxidized to simonkolleite in the $ZnCl_2$-rich atmosphere, which aligns with the conclusions of previous studies.[22,30] The presence of sufficient Cl^- and Zn^{2+} ions promotes the deposition of simonkolleite deposition (Equation (1)–(3)).

$$4Zn(OH)_2 + ZnCl_2 + H_2O \rightarrow Zn_5(OH)_8Cl_2 \cdot H_2O \quad (1)$$

$$4ZnO + ZnCl_2 + 5H_2O \rightarrow Zn_5(OH)_8Cl_2 \cdot H_2O \quad (2)$$

$$5Zn^{2+} + 8OH^- + 2Cl^- + H_2O \rightarrow Zn_5(OH)_8Cl_2 \cdot H_2O \quad (3)$$

Although the formation of simonkolleite may potentially occur through a one-step reaction (Equation (3)), prior investigations[22,31] suggest that its formation is more likely a result of the transformation of ZnO and ϵ-$Zn(OH)_2$ (Equation (1) and (2)). This formation mechanism is further supported by the subsequent NaCl-doping experiments. The formation of simonkolleite may be attributed to the properties of [BMIM]Cl. During the oxidation of metallic zinc, a fraction of imidazolium cations

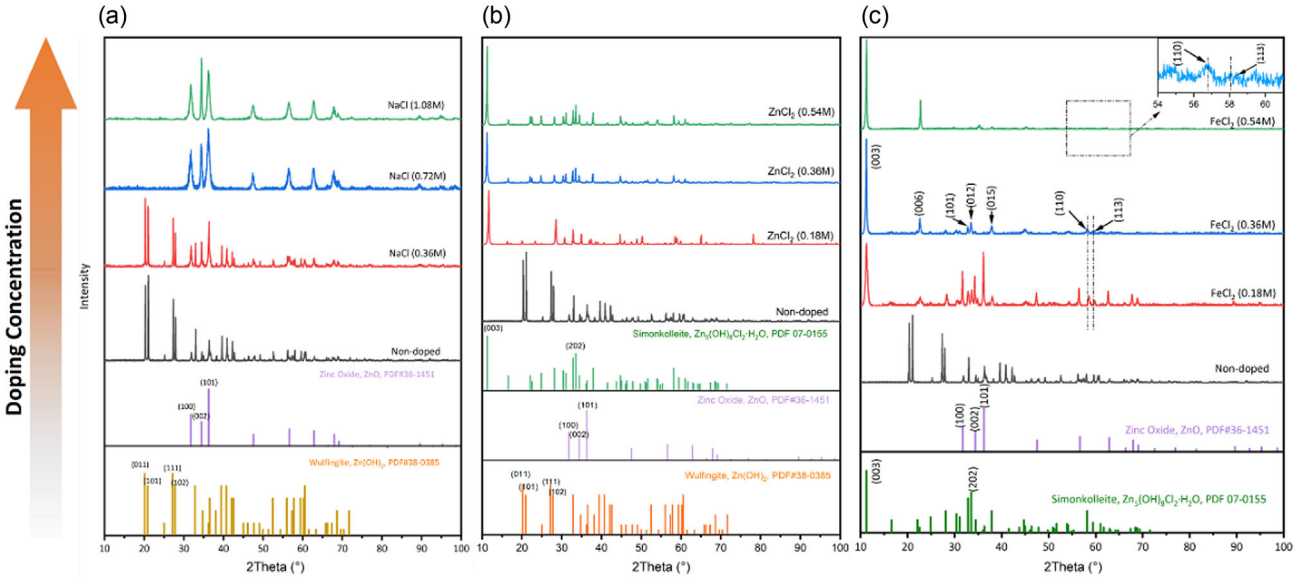

Figure 2. XRD patterns of a) NaCl-doping, b) $ZnCl_2$-doping, and c) $FeCl_2$-doping cases. The green, blue, red, and black curves indicate the product in four different concentrations from high to low. The reference peaks at the bottom indicate the possible components of the product, with some characteristic peaks labeled for identification.

$[BMIM]^+$ undergoes deprotonation to form [BMIM] Lewis bases (Figure 1b).[32,33] The existence of Lewis acid-base pairs allows the system to function as an effective buffer solution, maintaining a stable pH in a mild atmosphere, which is beneficial for the formation of Simokolleite. Furthermore, the IL [BMIM]Cl combined with $ZnCl_2$ may form a metastable $[BMIM]_2[ZnCl_2]$ complex structure,[34] which provides a high-concentration Zn environment essential for the formation of simonkolleite.[31] This helps regulating the precipitation process, preventing the rapid depletion of zinc ions. Previous research has shown that the direct oxidation of Zn by [BMIM]Cl, in the absence of any additives, predominantly results in the formation of ZnO and ϵ-$Zn(OH)_2$ species (Figure 2a, nondoped).[17,30] To determine the primary influence of Zn ions and chloride ions on simonkolleite formation, NaCl-doped cases were used as control, with equal concentrations.

In the cases of NaCl-doping, the Cl^- concentration was adjusted to a level commensurate with the corresponding $ZnCl_2$-doping cases. Therefore, the influence of Zn^{2+} can be eliminated. The XRD patterns of the product reveal entirely different signals (Figure 2a). In the presence of NaCl at high concentration (1.08 M), three distinct peaks [100] ($2\theta = 31.8°$), [002] ($2\theta = 34.5°$), [101] ($2\theta = 36.3°$) can be clearly identified. Aside from ZnO, there are virtually no additional impurity peaks. The peaks exhibit relatively broad profiles and low intensity, suggesting that the precipitated crystals have low crystallinity and a broad size distribution, further supported by the subsequent SEM analysis. A similar situation occurs in the mild concentration case (0.72 M). The specific peaks of ZnO between 30° and 40° are clearly visible. Hardly any other peaks are observed, and the existing peaks also exhibit a broad and short profile. It is worth noting that the peak intensity shows a slight variation when compared to the high-concentration case. The [101] peak at 36.3° is more intense than the [002] peak at 34.5°, which is the opposite of the pattern observed in the high-concentration cases. This could suggest a divergence in the orientation of crystal plane growth between the two cases, which will be further analyzed in the following section. The patterns also display distinct features in the low-concentration (0.36 M) and nondoped cases, compared with the previous two cases, where the most significant peaks are still attributed to $Zn(OH)_2$. The characteristic peaks, [011] ($2\theta = 20.1°$), [101] ($2\theta = 20.9°$), [111] ($2\theta = 27.2°$), and [102] ($2\theta = 27.8°$) display sharp and prominent profiles. In contrast, within the 2θ range of 30° to 40°, distinct ZnO peaks remain present; however, the intensity of ZnO is significantly weaker than that of $Zn(OH)_2$. In the nondoped case, the ZnO peaks further attenuate, with the remaining peaks primarily corresponding to zinc hydroxide.

As the NaCl concentration decreases from high to low, a notable transformation occurs in the synthesized products, shifting from a ZnO- to a $Zn(OH)_2$-dominant phase. It can be inferred that high concentrations of Cl^- ions play a positive role in the dehydration of ϵ-$Zn(OH)_2$. This effect may be attributed to the influence of doped NaCl on the polarity of the aqueous system. The higher concentration of NaCl increases the polarity, resulting in stronger interactions between $Zn(OH)_2$ and solvent molecules. This, in turn, promotes the cleavage of the oxygen-hydrogen bond in the zinc hydroxide molecule, leading to its transformation into ZnO. Compared with the $ZnCl_2$-doping cases, none of the cases involving NaCl-doping resulted in the generation of simonkolleite. This observation suggests that a high concentration of zinc ions is a necessary condition for the formation of simonkolleite.

Furthermore, in the NaCl-doping cases, H_2O molecules and hydroxide anions are present in sufficient amounts. The reaction rate is controlled by the presence of Zn^{2+} cations oxidized from

metallic Zn. The absence of simonkolleite formation in all NaCl-doping cases indicates that, under these conditions, the reaction kinetics are not governed by Equation (3). This supports the conclusion that, in $ZnCl_2$-doping cases, simonkolleite is more likely to form through the transformation of ZnO and $Zn(OH)_2$.

2.1.2. $FeCl_2$-Doping Cases

$FeCl_2$ was introduced as an additive to investigate the impact of iron ions on the morphology of the products. Similarly, the Cl^- ion concentration was maintained at the same level as in the previous cases. The product exhibits a yellow color that intensifies with an increase in the concentration of $FeCl_2$. The XRD patterns of this category of samples present unique profiles that are different from conventional minerals (Figure 2c). The pattern in the high-concentration case (0.54 M) is relatively monotonous. Only two significant peaks, located at 11.2° and 22.7°, are evident. Several relatively minor sloping peaks are distributed between 25° and 60°. No standard mineral XRD card entirely matches the observed experimental patterns. However, the XRD spectrum of the product closely aligns with the characteristics of a novel Zn–Fe LDH material, which exhibits a typical hydrotalcite-like structure similar to simonkolleite.[2,29,35,36] Therefore, the two distinct peaks can be attributed to the [001] crystal plane, analogous to that of simonkolleite. However, the subdued intensities of other peaks in the sample suggest that the crystals were highly oriented during growth. At moderate concentrations of $FeCl_2$ (0.36 M), the peaks at 11.2° and 22.7° remain sharp and intense. Additionally, specific peaks that were obscured in the high-concentration cases become more prominent. The triple peaks at 32.8°, 33.4°, and 37.9° correspond to the crystal planes [101], [012], [105] respectively. The presence of two characteristic peaks at 58.2° and 59.6° is also evident, although with slight shifts to lower angles. The low-concentration case exhibits more pronounced peaks that are characteristic of simonkolleite.[29] Moreover, distinct peaks corresponding to ZnO at 31.8° [100], 34.5° [002], and 36.3° [101] are observed in this pattern. This suggests that the product may consist of Fe-doped simonkolleite and ZnO. The Fe-doping cases indicate that the products of Zn oxidation are primarily simonkolleite-based crystals. It can be concluded that the introduction of Fe does not fundamentally alter the reaction mechanism of Zn oxidation by [BMIM]Cl. Some free Fe^{2+} ions are reduced by metallic Zn (Equation (4)). In this study, the added metallic Zn was three grams, corresponding to 0.046 M, even in the high-concentration Fe^{2+} cases (the maximum Fe^{2+} concentration was 0.027 M). This indicates that Zn^{2+} is released into the system much more rapidly than it is corroded by $[BMIM]^+$, resulting in an initial high concentration of Zn^{2+} available for the reaction. Therefore, the reaction mechanism for $FeCl_2$-doping likely reflects the trend observed in the $ZnCl_2$-doping cases. The XRD patterns exhibit similar features, especially in the low-concentration cases of $ZnCl_2$ and $FeCl_2$ (Figure 2a, red curve and Figure 2c, black curve). This similarity may explain the formation of simonkolleite in $FeCl_2$-doping cases, as opposed to the formation of ZnO or $Zn(OH)_2$ in the NaCl-doped systems.

$$Zn + Fe^{2+} \rightarrow Zn^{2+} + Fe \quad (4)$$

$$2H^+ + \frac{1}{2}O_2 + 2Fe^{2+} \rightarrow 2\,Fe^{3+} + H_2O \quad (5)$$

$$2Fe^{3+} + Fe \rightarrow 3Fe^{2+} \quad (6)$$

The introduction of $FeCl_2$ influences the subsequent crystal growth behavior, leading to distinct product characteristics observed in both mild- and high-concentration doping cases. Additionally, $FeCl_2$ may undergo oxidation by dissolved O_2 (Equation (5)). However, the reaction rate of Fe^{2+} formation is relatively low, becoming noticeable only when the Fe^{2+} concentration reaches 0.36 M.[37,38] Due to the competing reduction and oxidation processes, a significant portion of iron remains in the liquid phase as Fe^{2+} (Equation (6)). Moaty et al.[35] highlighted that the atomic radius and electronegativity of Fe^{2+} are closer to those of Zn^{2+} than Fe^{3+}, making Fe^{2+} ions more likely to substitute Zn atoms within the simonkolleite structure. As a result of Fe^{2+} doping, the interplanar spacing increases, causing a leftward shift in the [110] and [113] peaks.[39] Subsequently, Fe incorporated into the framework is oxidized to Fe^{3+}, ultimately contributing to the formation of Zn–Fe LDH crystal. When the Fe doping concentration reaches 0.54 M, the [003] peak becomes more prominent, distinctly differentiating from the mild- and low-concentration cases, as well as from pure simonkolleite. However, most other characteristic peaks are difficult to detect in the high-concentration case. It is worth noting that no separate iron-based phases, such as Fe_2O_3 or FeO phase, where identified in this study. However, it is possible that iron oxide exists as an amorphous form.

2.2. Morphology Analysis

2.2.1. NaCl-Doping Cases

During the synthesis process, variations in the concentration of doping ions significantly influence the morphological characteristics of the resulting crystals. In case of NaCl-doping, the product exhibits distinct shapes due to its $ZnO/Zn(OH)_2$-based crystalline nature. **Figure 3**a–d shows the morphologies observed in the NaCl-doped products. Predominantly, the crystals form agglomerated spherical structures. In contrast, the nondoped samples display diverse morphologies, including nanorods, nanospheres, and abundant irregular aggregates, with an average size of ≈250 nm (Figure 3a). Malaret et al.[17,40] reported on the oxidation of Zn in [BMIM]Cl solution. ϵ-$Zn(OH)_2$ initially forms sediment, which subsequently decomposes into ZnO. In the case of low concentration (NaCl = 0.36 M), the crystalline structures exhibit analogous morphologies compared to those observed in the nondoped case (Figure 3b), although the particle sizes are smaller (average size 120 nm), and aggregation is less pronounced. Rod-like crystals are still a majority, with spherical particles beginning to emerge (Figure S5, Supporting Information). This trend is further accentuated in the moderate and high concentration case (Figure 3c,d), where particles are relatively well-dispersed and exhibit a quasi-uniform spherical structure, with a size of ≈1 μm. Additionally, some porous and loosely coral-like aggregates are observed, likely resulting from the washing and drying process (Figure S6, Supporting Information).

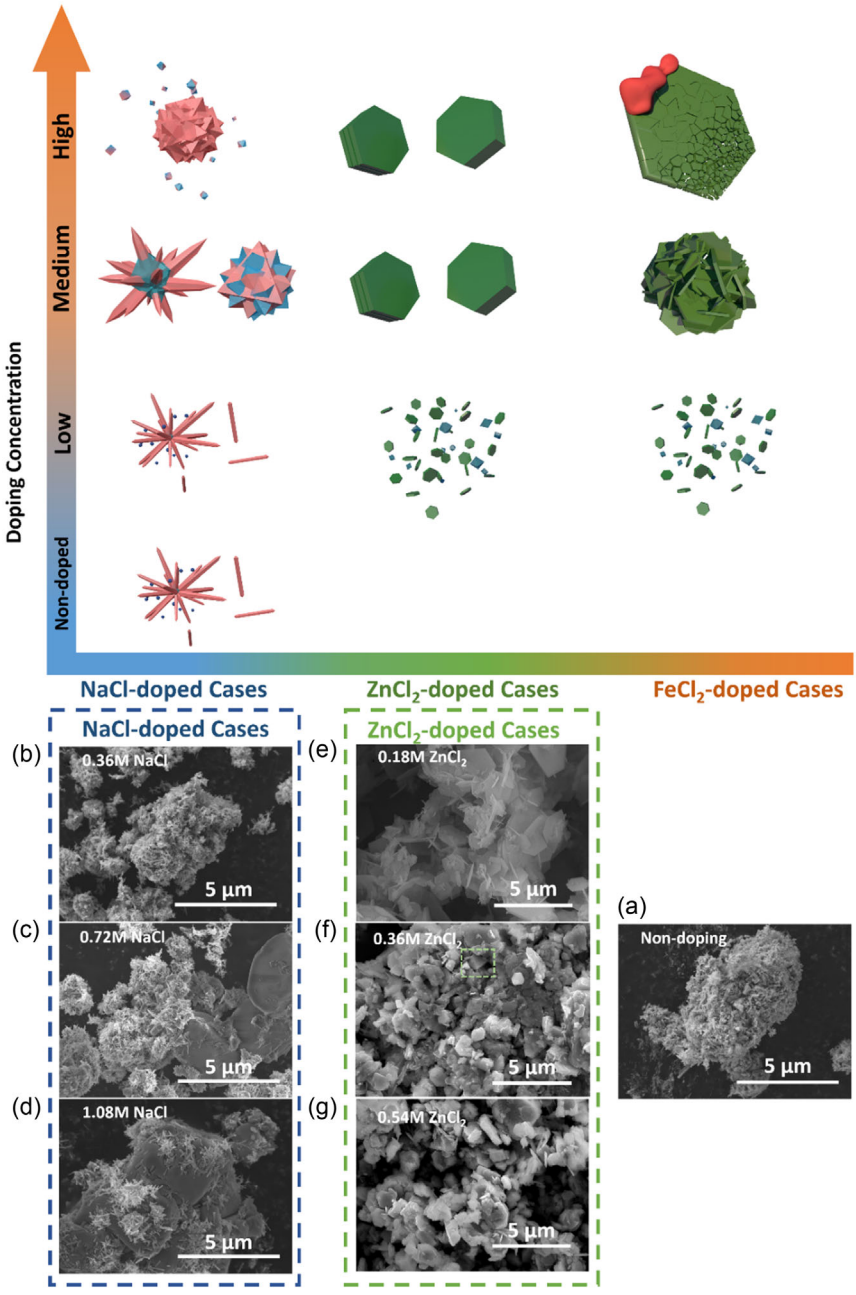

Figure 3. Schematic diagram of the morphology of the products under different doping ions and concentration conditions. $FeCl_2$-doping cases are presented separately in Section 2.2.3. The products were collected after reacting in [BMIM]Cl (10 %wt) with different concentrations of dopants for 24 h. a) No-doping case; b–d) NaCl-doping cases; e–g) $ZnCl_2$-doping cases; The green dashed box in (f) indicates a rare octahedral $Zn(OH)_2$ crystal.

The small particle size is hypothesized to result from Cl^- ions enhancing the polarity of the liquid system, thereby promoting the dehydration of $Zn(OH)_2$ to ZnO. Soluble Zn^{2+} ions are generated through the oxidation of metallic Zn form ϵ-$Zn(OH)_2$, due to the low solubility of $Zn(OH)_2$.[41] The transformation of ZnO is not kinetically favored without a high concentration of Cl^-. Thus, the process of ZnO formation often occurs over an extended timescale. The transformation of ϵ-$Zn(OH)_2$ to ZnO proceeds via two mechanisms: dissolution-precipitation and in situ crystallization.[42] In the dissolution-precipitation pathway, ZnO forms through the growth of Zn^{2+} ions released by the dissolution of $Zn(OH)_2$, followed by direct precipitation. This process exhibits anisotropic ZnO crystal growth, leading to distinctive needle-like and sea urchin-like morphologies. Cl^- ions, with their smaller ionic radius and higher chemical reactivity, can compete with hydroxide ions for binding with Zn^{2+}, potentially disrupting the stability of formed $Zn(OH)_2$.[43] High Cl^- concentrations promote the in situ $Zn(OH)_2$ crystallization,

effectively accelerating its transformation into ZnO. The impact of Cl^- is further enhanced in the high concentration of NaCl-doping case (NaCl = 1.08 M). The sample exhibits a significant presence of irregular particles (average size of ≈250 nm) due to the inhabited anisotropic growth. The elevated concentration of Cl^- and resulting high polarity facilitate particle growth and aggregation into microscale bulk structures.

2.2.2. $ZnCl_2$-Doping Cases

The products synthesized with $ZnCl_2$-doping exhibit the characteristic morphology of simonkolleite crystals, presenting as hexagonal plate-like structures (Figure 3). In the low-concentration doping cases, the particles exhibit thin hexagonal plate-like structures with well-defined edges (Figure 3e). The particle sizes exhibit a broad distribution, ranging from 500 nm to 3 μm, with an average diameter of ≈1.85 μm (here, the diameter of the hexagonal crystal is defined as the length of the diagonal connecting opposite corners of the hexagon). The thickness of an individual pellet is ≈35 nm, resulting in a high surface area-to-volume ratio. Moreover, a tendency for disordered coalescence into larger clusters is observed. It is worth noting that some small irregular particles adhere to the surface of the plate-like crystals.

As the $ZnCl_2$ doping concentration increases, noticeable differences in the particle size and thickness are observed (Figure 3f). The crystal diameter is generally smaller compared to the previous case, with an average diameter of ≈600 nm. Nonetheless, the thickness of the particles significantly increases, with variations in thickness ranging from 60 to 350 nm, with an average value of 200 nm. Although the bulk crystals larger than 1 μm continue to exhibit disordered stacking, a significant number of smaller crystals, approximately several hundred nanometers in size, align along their crystal plane and fuse to form larger, bulky crystals. Additionally, some relatively small crystals tend to agglomerate to crystal planes with larger particles stacking along the [001] plane. A limited number of octahedral bicone crystal structures have been observed, which are typically associated with $Zn(OH)_2$ crystal morphologies.

In the high-$ZnCl_2$-concentration doping case, the particles show similar morphologies compared to the mid-concentration case (Figure 3g). The crystals maintain the same hexagonal sheet-like structure with a larger diameter (700 nm) and thickness (250 nm). Additionally, the agglomeration between individual crystals appears to be more pronounced. Crystals can grow into large crystal clusters exceeding 5 μm in size through oriented stacking and fusion mechanisms.

The variations in morphology observed in the products from the three cases can be attributed to changes in the growth mechanisms of simonkolleite, which are induced by the concentration of the doping $ZnCl_2$. Simonkolleite formation is highly sensitive to solution pH and Zn^{2+} ion concentration. In nondoped and NaCl-doped cases, the introduced ions do not significantly affect the pH during the reaction process. The oxidation of metallic Zn by $[BMIM]^+$ ions causes the pH of the solution to shift from acidic to neutral or weakly alkaline conditions, which is thermodynamically favorable for the formation of ZnO.[31] Introducing $ZnCl_2$ into the IL leads to the hydrolysis of Zn^{2+} ions, resulting in an acidic environment.[44] Furthermore, the addition of $ZnCl_2$ provides the necessary precursor material for the formation of simonkolleite. Pelicano et al.[45] indicated that one of the conditions for simonkolleite formation is the concentration of Zn^{2+} exceeding 0.01 M. This study confirms this condition, suggesting that the Zn^{2+} released by the IL [BMIM]Cl alone is insufficient to produce simonkolleite under the experimental conditions employed. Specifically, in the case of low $ZnCl_2$ concentrations (0.18 M), the reaction conditions are relatively mild, and the growth of simonkolleite follows a monomer-to-monomer growth mechanism, relying on the deposition of free Zn^{2+} from the liquid phase. As a result, the formed particles exhibit well-defined crystals with relatively smooth surfaces. The $[BMIM]^+$ ions, with their hydrophobic tails, may interact with Zn and adsorb onto the polar plane [001] of simonkolleite, hindering its growth along the *c*-axis direction. Therefore, the morphology of the crystal presents an extremely thin thickness with a wide, flat plane. However, Malaret et al. indicate that simonkolleite is more likely to transform from $Zn(OH)_2$ as the precursor.[17,46] This behavior is not prominently observed in the current case, and it is speculated to primarily occur during the crystal nucleation stage. The irregular small particles distributed throughout the sample are presumed to be the $Zn(OH)_2$, although this remains unverified.

With a further increase in the $ZnCl_2$ concentration (0.36 and 0.54 M), the crystallization of simonkolleite is driven by the nucleation process, resulting in a rapid crystal growth. Nanocrystals with diameters smaller than 100 nm pervade the liquid phase, leading to inevitable mutual contact and aggregation.[47] Meanwhile, the high concentration of $ZnCl_2$ prompts the polarity of the system, intensifying the fusion between the particles. In a polar environment, the polar surfaces of simonkolleite readily attract each other, promoting aggregation into thicker and larger crystals through face-to-face interaction.[22] Conversely, a small amount of $Zn(OH)_2$ crystals has also been observed, confirming the transformation route from $Zn(OH)_2$ to simonkolleite. This may occur because excessive $ZnCl_2$ causes $Zn(OH)_2$ to precipitate once the Zn^{2+} required for Simonkellaite growth has been consumed. This phenomenon is significant in the $ZnCl_2$ high concentrations regime. In this scenario, a considerable amount of simonkolleite forms large bulky crystal covered by hexagonal plate-like crystals on each facet. Octahedral $Zn(OH)_2$ crystals are speculated to undergo surface transformation into simonkolleite, eventually forming distinctive aggregated clusters.

2.2.3. $FeCl_2$-Doping Cases

$FeCl_2$-doping cases exhibit the most complex morphologies in this study. As discussed in the previous section, the products are mainly composed of Zn–Fe LDH, while retaining some features of simonkolleite crystals. Some discernible single crystals still exhibit the hexagonal sheet-like shape which is characteristic of $ZnCl_2$-doping cases, although this morphology is less pronounced at the microscale. Based on measurements from the SEM images (**Figure 4**a–c, S7a–c, Supporting Information), the thickness of the nanosheets is relatively thin, with values below 100 nm. As the concentration of added $FeCl_2$ increases, the thickness of the particles also increases, ranging from 25 nm at 0.18 M $FeCl_2$ doping to 100 nm at 0.54 M $FeCl_2$ doping.

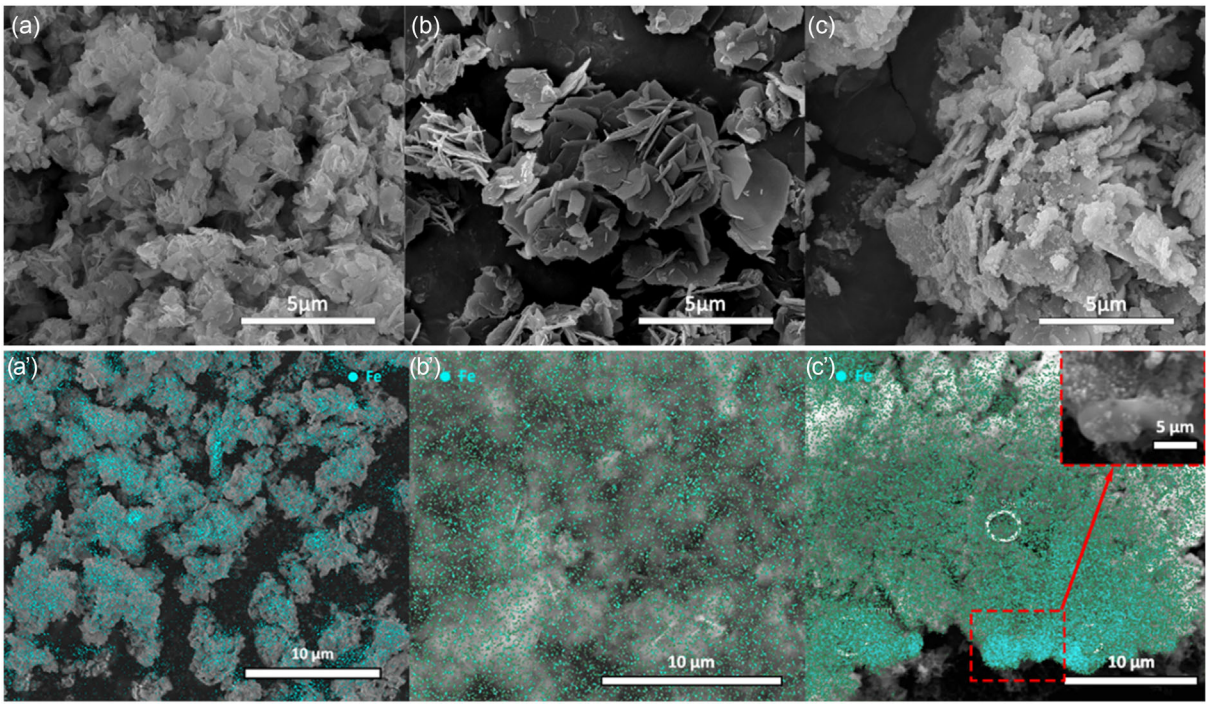

Figure 4. SEM images and EDS analysis patterns of the $FeCl_2$-doping group's product. Products were synthesized in [BMIM]Cl (10 %wt) with different concentrations of $FeCl_2$ doping for 24 h; a) 0.18 M $FeCl_2$-doping; b) 0.36 M $FeCl_2$-doping; and c) 0.54 M $FeCl_2$-doping; a–c) The images in the top row illustrate the crystal morphologies at a magnification of 20 000 times; a'–c') energy dispersive X-ray spectroscopy (EDX) analysis patterns for the corresponding samples. The images only show the signals of Fe (blue). Fe ratio for three cases is a) 6.47, b) 1.71, and c) 0.20, respectively.

In the low-concentration doping case ($FeCl_2 = 0.18$ M), spherical and granular agglomerates are observed between the hexagonal sheets of single-crystal particles at the microscale (Figure 4a). This arrangement appears more as disordered stacking compared to the face-to-face alignment observed in the previous case (Figure 3f,g). Meanwhile, some tiny irregular particles can also be observed, which are considered to be a dehydration product ZnO, derived from the simonkolleite precursor $Zn(OH)_2$.[17] With moderate $FeCl_2$ doping, the formed crystals exhibit clearer boundaries and fewer clusters of spherical aggregates (Figure 4b). It can be found that a large tablet-shaped crystal is composed of multiple small sheets stacking and merging, indicating a shift in the aggregation mechanism. There are two types of assembly behavior between the single nanosheets, namely, 1) large nanosheets interlace in a helical arrangement, forming a 'desert rose' morphology; 2) small nanosheets align and adhere to the large flat surface, thickening along the [001] direction. Similarly, in the high-concentration $FeCl_2$ doping case, the product presents lamellar morphologies rather than granular structures at the microscale. However, the lamellae are composed of spherical particles with an average size of ≈80 nm, resulting in the formation of lamellar crystals with a rough surface and the presence of defects. In some positions, cavities are observed (Figure S7c, Supporting Information), which can be described as resembling "dead leaves." Meanwhile, the nanosheets also adhere to some scattered nanospheres, which are presumed to be fragments separated from large crystals, suggesting that the mechanical strength of the crystals is relatively low. Additionally, some crystals are observed to be covered by amorphous particles, which are speculated to be iron oxides.

The above cases indicate that the Fe–Zn ratio is essential in forming Zn–Fe LDH. Introducing Fe^{2+} significantly affects the crystallization process and final morphology. The EDX analysis (Figure 4a'–c') confirms that the doped Fe content increases as the $FeCl_2$ concentration increases. The distribution in the low-concentration case shows a core enrichment state (Figure 4a'). Contrastingly, Fe is distributed more evenly on the hexagonal Zn-based nanosheets in the middle and high concentration cases (Figure 4b',c').

A low concentration of Fe^{2+} is rapidly consumed in the reaction with metallic zinc. The adsorption of [BMIM]Cl provides a metastable environment for the reduced Fe particles,[48] thus maintaining a low concentration of Fe^{2+} ions. At this point, the liquid phase can be considered doped with an equivalent amount of $ZnCl_2$. A significant amount of reduced Fe powders provides nuclei for simonkolleite nucleation, which results in crystal growth as a nucleation-dominated stage for an extended period. Therefore, the formed tiny nanosheets tend to agglomerate as a spherical granule to reduce surface tension for a thermodynamically stable state. Due to the encapsulation of $BMIM^+$ ions on the polar surfaces, the anisotropy between single crystals cannot be well expressed. Consequently, the clusters form through the disordered stacking of small nanosheets. Simultaneously, some small irregular spheres are likely amorphous precursor $Zn(OH)_2$ and ZnO, which are generated during the aging process.[49]

As the concentration of $FeCl_2$ is increased to 0.36 M, a significant amount of free Fe^{2+} ions remains in the liquid phase. As discussed earlier, these Fe^{2+} ions can systematically and periodically replace some of the Zn atoms in the simonkolleite structure, leading to the formation of a single-phase Zn–Fe(II) LDH.[35,39] Hence, the resulting microplates exhibit well-crystallized structures with smooth surfaces with a Zn-to-Fe ratio of ≈1.71, maintaining the layered structure of the material.

During the crystallization maturation process, the high polarity of the solution and the presence of a large number of existing crystals lead to a phenomenon where single crystals engage in self-assembly. This process facilitates the fusion growth of the crystals, ultimately minimizing the surface energy. Two strategies for self-assembly were observed in the formation of Zn–Fe(II) LDH. Initially, a single crystal aggregates into a spirally arranged structure, resembling a "desert rose" (**Figure 5**). During the crystal growth, the surface-doped Fe^{2+} may undergo pre-oxidation. As a result, the Fe^{3+} ions, which have smaller ionic radius than Fe^{2+}, may occupy certain positions, causing a distortion or kink in the crystal structure. At these sites, the growth of another hexagonal single crystal may occur, or single crystals may adhere and fuse together. The fusion, driven by multiple kinks on the crystal facets, causes the hexagonal sheets to agglomerate into desert-rose-like spherical shapes, thereby minimizing the surface energy. Another observed form of assembly is oriented attachment, where smaller crystals align face-to-face on the surface of a larger crystal, promoting growth along the *c*-axis and leading to an increase of the thickness of the crystal.[50,51]

However, the excessive introduction of $FeCl_2$ results in the supersaturation of the solution with Fe^{2+}; some of the Fe^{2+} cations precipitate and undergo premature oxidation to Fe^{3+}. This oxidation can significantly alter the pH of the solution, preventing the coprecipitation of Fe and Zn. Simultaneously, Fe^{3+} cannot be effectively incorporated into the layered structure.[29,49] As a result, the number of layered crystals is reduced, and their size becomes smaller compared to the previous cases. Additionally, supersaturated Fe^{3+} may precipitate as amorphous iron hydroxide or oxide,[29] which can adhere to the surface and to the edges of the platy crystals, hindering further crystal growth to form rough surfaces with pores.

The $FeCl_2$-doping cases were also characterized by Brunauer-Emmett-Teller for surface area measurement (Table S2, Supporting Information). At the doping concentration of 0.18 M Fe, the product primarily consists of simonkelleite crystals prone to significant agglomeration, resulting in the smallest surface area. As the Fe concentration increases, larger and more stable simonkolleite lamellar crystals form, contributing to a substantial increase in surface area. As the concentration of Fe doping increases to a certain threshold (0.36 M), the stability of LDH is compromised. A significant number of defects and even fractures appear on the layered crystals, leading to a substantial increase in the specific surface area.

2.3. Precipitation Rate and Crystallization Mechanism

2.3.1. Models for QCM Response for Zn-Based LDH Growth

The mechanism of Zn–Fe LDH formation can be further investigated using the QCMD method, which leverages the piezoelectric effect of quartz to measure minute mass changes.[52] The detailed experimental design and theoretical derivation of the models of QCMD response for Zn-based LDH growth are provided in Supporting Information S2. In this study, a quartz piece was immersed in the liquid phase, assuming uniform

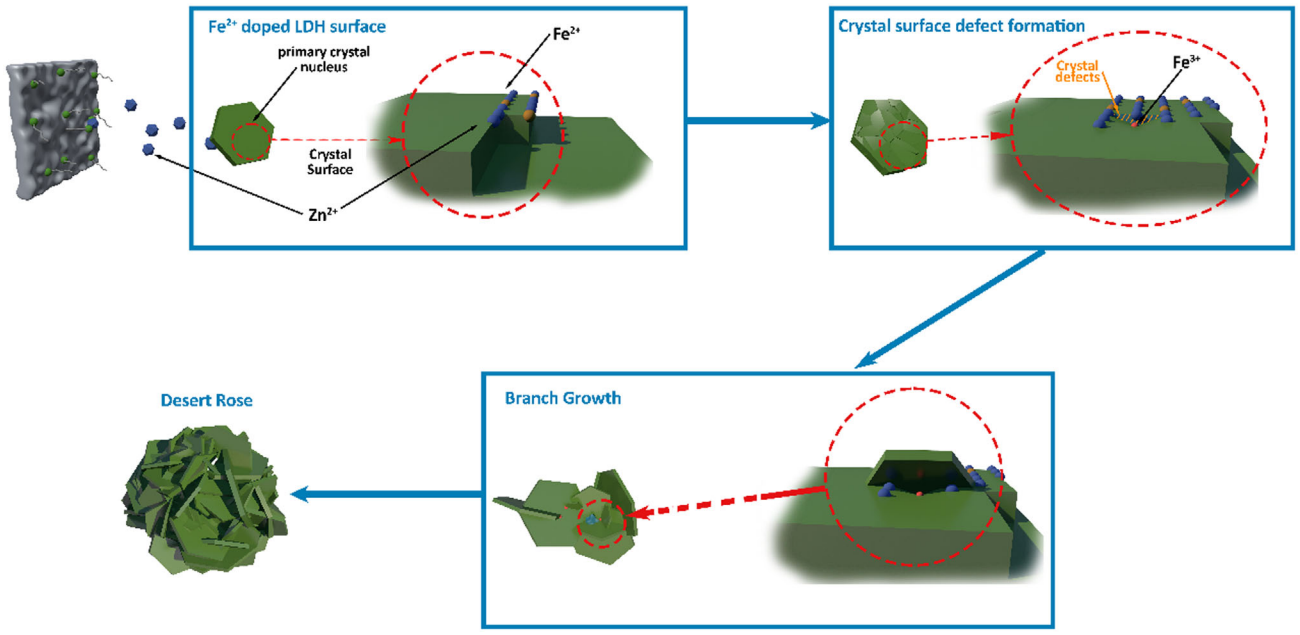

Figure 5. Schematic diagram of the formation mechanism of the "desert rose" morphology; the green surface indicates the layered crystal. Blue spheres correspond to Zn^{2+}; yellow spheres correspond to Fe^{2+}; and red spheres correspond to Fe^{3+}. After oxidation, the ionic radius of Fe^{3+} decreases, and its electronegativity increases. With stress, defects appear on the crystal surface, providing the possibility of branches on the [001] facet.

precipitation on its surface. The quartz sensor was removed every hour to measure its resonant frequency and dissipation factors in the deionized water, ensuring the elimination of interfering factors in the stock solution. The relationship between the frequency change in QCMD and deposition mass is described by the Sauerbrey equation:[53]

$$\Delta m = -C \cdot \frac{\Delta f}{n} \tag{7}$$

where Δm is the mass changes of quartz on the unit area (the reported unit is ng cm^{-2}), mainly resulting from the deposited substance, Δf is the observed frequency changes, C is the mass sensitivity constant, (17.7 ng cm^{-2} Hz^{-1}), and n is the odd overtone number ($n = 3$).

Further analysis of the dissipation factor reveals two primary causes of energy losses: 1) energy dissipation from the continuous layer's loss modulus (G''), and 2) energy loss due to surface roughness. The first factor is considered negligible due to the rigidity of the microcrystals and the small thickness of the layer. Therefore, only the roughness effect is significant, which describes energy loss from the interaction between the quartz and the attached mass during oscillation. Based on the previous SEM images, the crystals attached to the quartz surface can be simplified as a liquid-crystal interface that follows a Gaussian random distribution. This is regarded as a shallow roughness model with low feature height h_r and long feature l_r width (Figure S3, Supporting Information). Referring to the derivation proposed by Daikhin et al.[54] for the Gaussian random distribution of the profile of liquid-crystal interface, the surface impedance Z_L^* can be obtained by considering limiting scenarios. These include the dynamic viscosity η_l, the density of the liquid ρ_l, the frequency of the acoustic wave ω, the acoustic decay length in viscous flow δ, and the roughness characteristic height h_r with in-plane parameter l_r (SI SE 1–6). In this study, calculations were obtained based on the dissipation measured under the third harmonic (frequency of harmonic is $\approx 3 \times 5$ MHz) to ensure the reliability of the data. Under this condition, the impedance equation can be further simplified into the following form, as described by Daikhin et al.[54]

$$h_r = \sqrt{\frac{D}{D_0} - 1} \cdot \sqrt{\frac{\eta_l}{\rho_l \omega}} \tag{8}$$

Therefore, the precipitation state on the quartz can be monitored and quantified by simply measuring the resonance frequency f and its dissipation D. The collected data was converted to deposition mass Δm and roughness parameter h_r and plotted in Figure S3, Supporting Information. The graph does not display deposition mass and roughness data for this sample because no deposition was observed on the quartz during the first 6 h for the nondoped cases.

2.3.2. Deposition Mass and Roughness

According to classical crystallization theory, crystallization occurs when the solution reaches supersaturation, followed by nucleation and crystal growth.[55,56] Therefore, the deposition mass measured by QCM over time can be roughly divided into three stages: prenucleation, nucleation-dominated, and crystal growth-dominated. In the NaCl-doping cases, the changes in deposition mass effectively capture the entire process. At the early stage, the detected mass remains low. In the case of high NaCl concentration, the prenucleation stage lasts for the first 5 h, during which [BMIM]Cl oxidizes the metallic zinc to increase the concentration of Zn^{2+} to supersaturation levels. Similarly, the roughness h_r follows the same trend. This remains at a low level, indicating that only a small amount of precipitation has settled on the quartz surface, thus maintaining its relatively smooth texture. As the amount of introduced NaCl decreases, the oxidation reaction is enhanced, reducing the prenucleation stage to $\approx$3 h. Subsequently, a significant increase in the deposition mass occurs between the fourth and the fifth hours, indicating that the reaction system has entered the nucleation stage. By the sixth hour, the rate of mass increase noticeably slows down, indicating a decrease in Zn^{2+} supersaturation due to its consumption during nucleation. This highlights the transition to the crystal growth-dominated stage. The roughness of both cases shows a similar monotonic increase over time. It can be observed that a high concentration of NaCl does not facilitate the occurrence of precipitation. Conversely, medium or low concentrations of NaCl promote precipitation during the first 6 h.

In case of $ZnCl_2$ doping, the mass change curve exhibits a slightly more complex behavior. Overall, all three cases show a consistent increasing trend from the start of the measurement, eventually reaching a similar order of magnitude. The final mass deposited on quartz increases with $ZnCl_2$ concentration by the sixth hour. It is worth noting that at high concentrations, the deposited mass remains nearly constant between the second and the fourth hour. The high-concentration case exhibits the lowest surface roughness throughout the measurement period. In the medium-concentration case, the roughness increases in parallel with the deposition mass, while the low-concentration case shows a rapid rise in roughness during the first 2 h. These observations suggest that the sediment in the $ZnCl_2$-doping scenarios may undergo a transformation during the process. The introduction of $ZnCl_2$ serves as an efficient precursor for precipitation, effectively bypassing a prolonged prenucleation stage. With the oxidation of metallic Zn, the pH of the solution increases from weak acid to base, favoring the formation of $Zn(OH)_2$ nuclei. This nucleation process contributes to an increase in surface roughness. However, the high concentration of Cl^- and Zn^{2+} released during oxidation thermodynamically promotes the formation of simonkolleite. Consequently, simonkolleite competitively precipitates alongside $Zn(OH)_2$. When the Zn^{2+} ion concentration in the liquid phase becomes insufficient, $Zn(OH)_2$ undergoes redissolution and support the crystallization of simonkolleite.[31] While nucleation partially contributes to surface roughness, the primary driver of roughness increase is crystal growth. Accordingly, it can be inferred that nucleation remains the dominant process in the high-concentration case, whereas in the medium- and low-concentration cases, the process transitions from nucleation to crystal growth.

The $FeCl_2$-doping cases exhibit a significant difference from the other scenarios, with deposition masses rapidly increased to exceed 600 ng cm^{-2} by the sixth hour, compared to less than 250 ng cm^{-2} in the other cases. The low concentration of $FeCl_2$-doping case achieves the highest deposition rate surpassing

500 ng cm^{-2} within the first 2 h. Following this initial surge, the deposition mass linearly increases at a precipitation rate of 150 ng cm^{-2} h^{-1} to exceed 1300 ng cm^{-2} by the sixth hour. In this case, the roughness reaches a steady value after the third hour. The medium-concentration $FeCl_2$-doping case exhibits a similar rapid increase in deposition mass during the first 2 h. Subsequently, the growth rate slows until the fifth hour, after which it surges dramatically, reaching 1100 ng cm^{-2} by the sixth hour. During the first 2 h, the roughness increases significantly due to nucleation while showing a noticeable decrease in the third hour, as a result of the possible shift in the dominant process. In contrast, introducing a high concentration of $FeCl_2$ results in the slowest deposition rate among the three cases.

Based on the evidence above, the mechanism of Fe–Zn LDH formation appears analogous to that of simonkolleite. It is hypothesized that $Zn(OH)_2$ forms as the primary kinetically favored product and, afterward, is transformed into Zn–Fe LDH by Fe^{2+} incorporated into brucite-like trioctahedral hydroxide layers.[29] In the low-concentration case, Fe^{2+} ions facilitate the oxidation process of Zn to Zn^{2+}, resulting in the formation of simonkolleite (**Figure 6**).

2.3.3. Mechanism of Product Formation

This study investigates the impact of Cl^-, Zn^{2+}, and Fe^{2+} ions on the crystal growth mechanism. The findings reveal that their impact increases in the order $Cl^- < Zn^{2+} < Fe^2$. Collectively, these ions regulate the reaction and crystal growth mechanisms by adjusting oxidation reaction rate, liquid-phase ion environment, and polarity, ultimately determining the composition and the morphology of the final products. The following chapter provides a summary of the mechanism underlying NaCl, $ZnCl_2$, and $FeCl_2$ doping.

Crystal Growth Mechanism in NaCl-Doping Cases: The primary role of NaCl is to adjust the polarity of the solution and promote the corrosion of metallic Zn in the IL. Initially, metallic Zn is corroded by acidic $[BMIM]^+$ ions to release Zn^{2+} ions.[17] In the absence of additives, the kinetic of Zn oxidation is slow, resulting in a low concentration of Zn^{2+}.[43,57] $Zn(OH)_2$ precipitates and gradually dehydrates into ZnO as the pH increases.[58] The growth of the formed ZnO is driven by Zn^{2+} ions freely available in the liquid phase or those released from redissolved $Zn(OH)_2$. This process promotes the development of rod-shaped

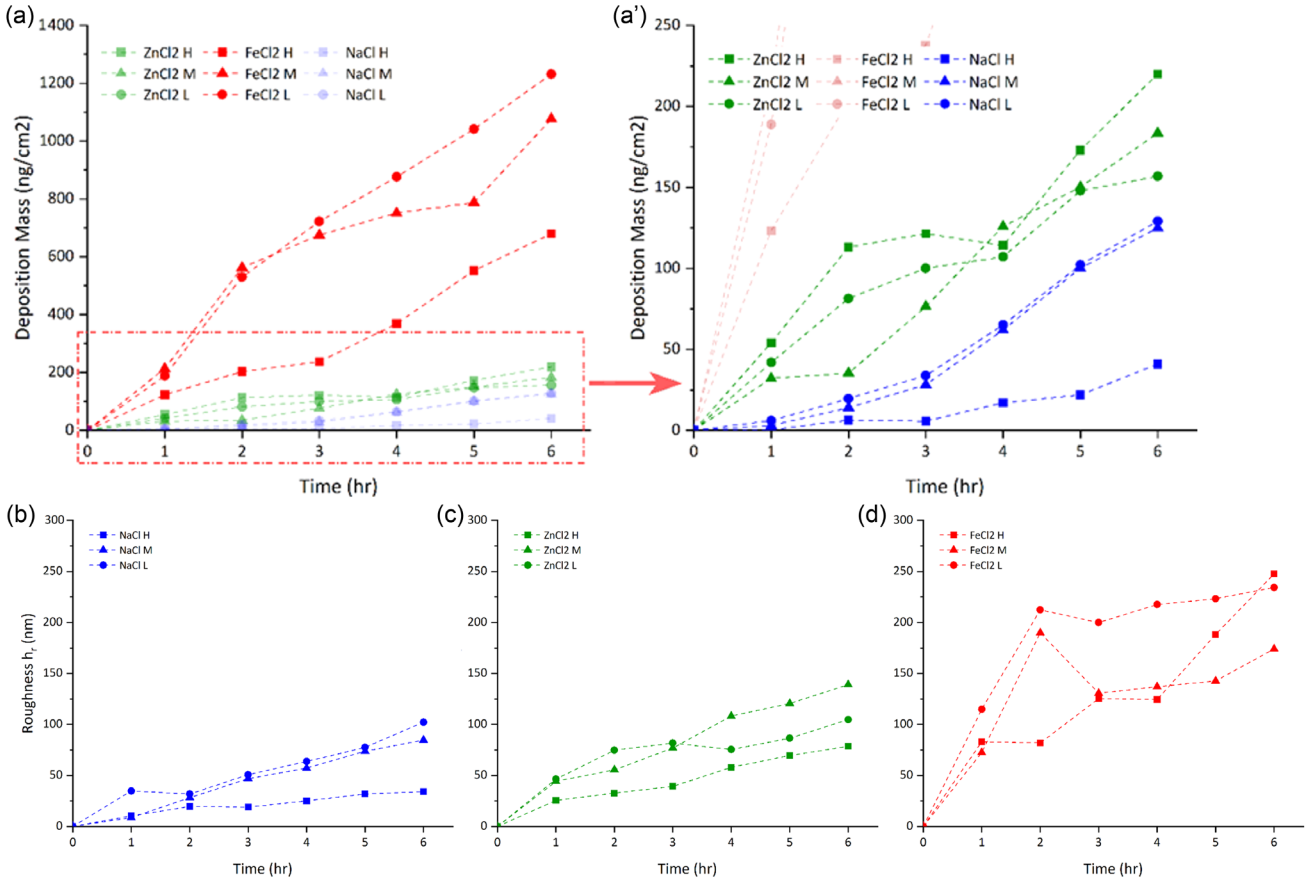

Figure 6. a,a') Deposition mass as a function of time for Zn reacting in [BMIM]Cl solution with metal chloride doping. The colors blue, green, and red, represent NaCl, $ZnCl_2$, and $FeCl_2$, respectively. Squares, triangles, and circles stand for the doping concentration, which ranges from high to low. The lines are only for guiding the eye. Due to the significant difference in scale between the $FeCl_2$ case and the other groups, the images are split into two figures with different scales. b–d) The diagram of roughness versus time in three groups. Squares, triangles, and circles indicate the doping concentration for NaCl (blue), $ZnCl_2$ (green), and $FeCl_2$ (red), ranging from high to low.

and needlelike ZnO crystals with a relatively high length-to-width ratio.[42] As a result, the product exhibits diverse morphologies, including needlelike, sea urchin-like, nanorod, and spherical shapes, comprising a mixture of $Zn(OH)_2$ and ZnO.

The introduction of NaCl creates a high-concentration environment of Cl^-, which improves the corrosion of metallic Zn.[59] ZnO growth predominantly follows a mechanism where $Zn(OH)_2$ binds to the surface and subsequently dehydrates.[41,42] Consequently, the final product primarily comprises irregularly shaped particle aggregates, with ZnO as the dominant phase (**Figure 7**).

Crystal Growth Mechanism in $ZnCl_2$-Doping Cases: Similar to NaCl doping, the introduction of $ZnCl_2$ leads to the initial formation of $Zn(OH)_2$. However, the addition of Zn^{2+} ions limits the initial prenucleation period associated with the corrosion of metallic Zn, allowing zinc ions to directly reach supersaturation without the delay typically observed in the absence of Zn^{2+}. When the pH of the solution rises to neutral, the precipitation process initiates. Similarly, a sufficiently high concentration of Zn^{2+} (>0.01 M) results in the formation of simonkolleite as the thermodynamically favored product.[45] As simonkolleite crystal growth progresses, the consumption of Zn^{2+} leads to a decrease in supersaturation, resulting in the transition to a crystal growth-dominated mechanism. The IL wrapped around the [001] polar facets of simonkolleite inhibits its growth along the *c*-axis.[60–62] Consequently, the final product consists of hexagonal thin nanosheets of simonkolleite with a high aspect ratio.

Furthermore, a higher concentration of $ZnCl_2$ (>0.36 M) leads to crystallization under a nucleation-dominated process with sustained high supersaturation levels over an extended period. This prolonged nucleation stage results in the formation of a large number of nuclei that are dispersed throughout the liquid phase. In this scenario, crystal growth may proceed via nonclassical pathways, such as oriented attachment. The increased polarity of the solution weakens the IL's confinement effect, leading to the formation of smaller particles that are thicker compared to the larger, thinner crystals observed in the low-concentration case (**Figure 8**).[22,63]

Crystal Growth Mechanism in $FeCl_2$-Doping Cases: The presence of Fe^{2+} ions significantly accelerates the corrosion rate of Zn in the IL. During the initial stage, Fe^{2+} rapidly oxidizes Zn^{2+}, while itself being reduced to metallic Fe powder. Additionally, this process generates a small number of free Fe^{2+} ions, which further promote the oxidation of metallic Zn in the subsequent stages of the reaction.[49] This behavior sustains a high concentration of Zn^{2+} ions in the liquid phase over an extended period, promoting nucleation-dominated crystallization processes. Additionally, the presence of iron facilitates the earlier transformation of $Zn(OH)_2$ into double-layer hydroxides. At a low concentration of Fe^{2+} (0.18 M), its impact on the product composition is minimal, with simonkolleite remaining the dominant phase. However, the reduced iron particles can act as nucleation sites or carriers, promoting the aggregation of simonkolleite into clusters. As a result, the final product exhibits a morphology characterized by hexagonal sheets that are largely aggregated into clusters.

A moderate concentration of $FeCl_2$ (0.36 M) accelerates the oxidation of metallic zinc and maintains some Fe^{2+} ions in the liquid phase as active free species. These ions can be incorporated into $Zn(OH)_2$ to form a uniform Zn–Fe LDH phase. The resulting Zn–Fe LDH displays a typical lamellar structure with a large surface area and thin layers.[29] During the formation of Zn–Fe LDH, a self-assembly behavior occurs among single crystals to minimize surface energy. Initially, amorphous NPs are formed, which are hypothesized to act as the precursor of a simonkolleite-based compound. With the assistance of $[BMIM]^+$ ions acting as templates and the anisotropic growth of the crystals, single crystals preferentially form hexagonal

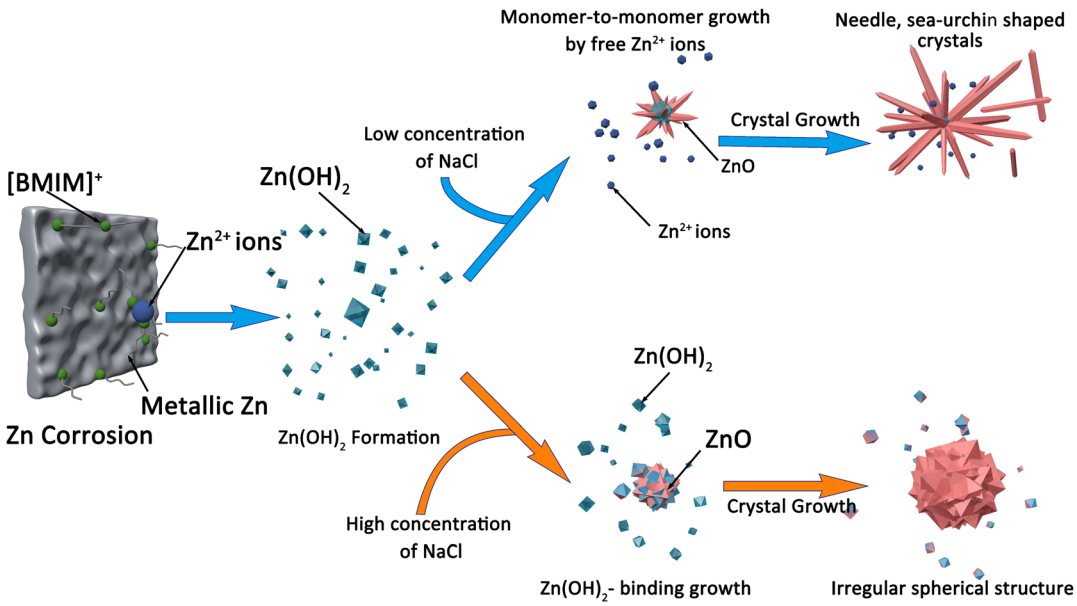

Figure 7. Proposed mechanism of zinc oxide crystal growth mechanism in NaCl-doping cases. The blue spheres represent Zn^{2+} ions, the light blue octahedrons represent the $Zn(OH)_2$ crystals, and the pink crystals represent ZnO.

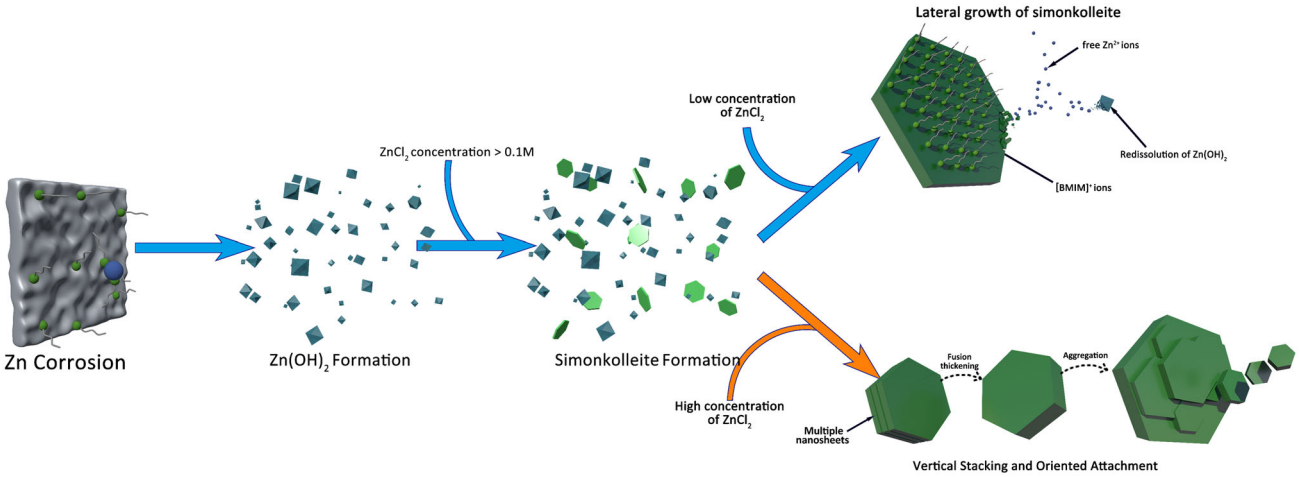

Figure 8. Proposed mechanism of zinc oxide crystal growth mechanism in the $ZnCl_2$-doping cases.

nanosheets similar to simonkolleite. However, the layered structure is prone to kinks, particularly when a small part of the doped Fe^{2+} is oxidized to Fe^{3+}. This introduces the formation of more complex topological structures in the Zn–Fe LDH, differing from the simpler nanosheet structures observed in the $ZnCl_2$-doping cases. The hexagonal nanosheets self-assemble in a spiral configuration, with the initially nucleated amorphous precursor serving as the core. Simultaneously, new helical centers form at the kinks within the structure, facilitating growth to minimize surface energy. This self-assembly process ultimately leads to the formation of the "desert rose" structural morphology.[64,65]

Conversely, a high concentration of $FeCl_2$ negatively impacts the formation of the product. Excess Fe^{2+} is prematurely oxidized to Fe^{3+}, leading to a decrease in the pH of the solution, which is unfavorable for LDH precipitation. The Fe^{3+} ions that cannot be incorporated into Zn–Fe LDH may form amorphous Fe oxides, which hinder crystal growth. Furthermore, incorporating Fe^{2+} into the Zn–Fe LDH crystal, followed by its early oxidation to Fe^{3+}, exacerbates lattice distortion due to the significant difference in atomic radii. This distortion disrupts the normal growth of Zn–Fe LDH.[38,66] The resulting increased internal stress within the lattice induces numerous defects and fractures on the crystal surfaces. This ultimately leads to the formation of fragmented, irregular nanosheets that are mixed with amorphous iron oxides (**Figure 9**).

2.4. Evaluation of the Photocatalytic Performance

Photocatalytic hydrogen production experiments were conducted under identical operating conditions, as described in the Supporting Information, using Zn–Fe LDH materials doped with different iron concentrations. **Figure 10** shows the H_2 production rate in the presence of methanol as a sacrificial agent and the LDH synthesized using different concentrations of $FeCl_2$. It is worth noting that the photocatalytic experiments were conducted without the use of any co-catalyst. Increasing the concentration of $FeCl_2$ during the photocatalyst synthesis in the range 0.18–0.45 M results in an increase of the hydrogen production rate. The samples prepared using $FeCl_2$ concentrations of 0.54 and 0.45 M exhibit a photocatalytic activity approximately five times higher than commercial zinc oxide. A possible mechanism for the photo-oxidation of methanol into formaldehyde, leading to hydrogen production, is described by the following equations, where e^- and h^+ represent the negative and positive charge carriers:

$$ZnFe - LDH + hv \rightarrow e^- + h^+ \quad (9)$$

$$e^- + h^+ \rightarrow \text{heat and light} \quad (10)$$

$$CH_3OH + h^+ \rightarrow CH_3O\cdot + H^+ \quad (11)$$

$$CH_3O\cdot + h^+ \rightarrow CH_2O + H^+ \quad (12)$$

$$2H^+ + 2e^- \rightarrow H_2 \quad (13)$$

Photogenerated holes oxidize methanol to form a methoxy radical, which is further oxidized to formaldehyde. Additionally, formic acid and carbon dioxide can be formed through oxidation of formaldehyde.

The specific surface area of the LDH hexagonal lamellar structure increases as more Fe ions are substituted into the backbone, which could potentially lead to an increase in the number of active sites for methanol adsorption. As reported in Figure 4, the increase in $FeCl_2$ concentration during the synthesis correlates with a rise in the doped Fe content of LDH with more uniform Fe distributions at high concentrations. Figure 10 reveals that the increase of uniformly dispersed Fe ion doping in the photocatalyst within the explored range has a positive impact on the hydrogen production rate. Fe^{2+} has been proven to be an effective dopant due to its interaction with the photogenerated electrons within the semiconductor, resulting in a decrease in the electron-hole recombination rate. However, at doping levels higher than 0.45 M, the excessive coverage of LDH surface reduces the light energy adsorbed by the photocatalyst. Additionally, at higher doping concentrations, Fe^{2+} is increasingly oxidized to Fe^{3+}, resulting in the formation of amorphous iron oxide. According to previous studies,[12] Fe_2O_3 negatively affects the photocatalyst's performance by favoring the recombination of photogenerated electron-hole pairs.

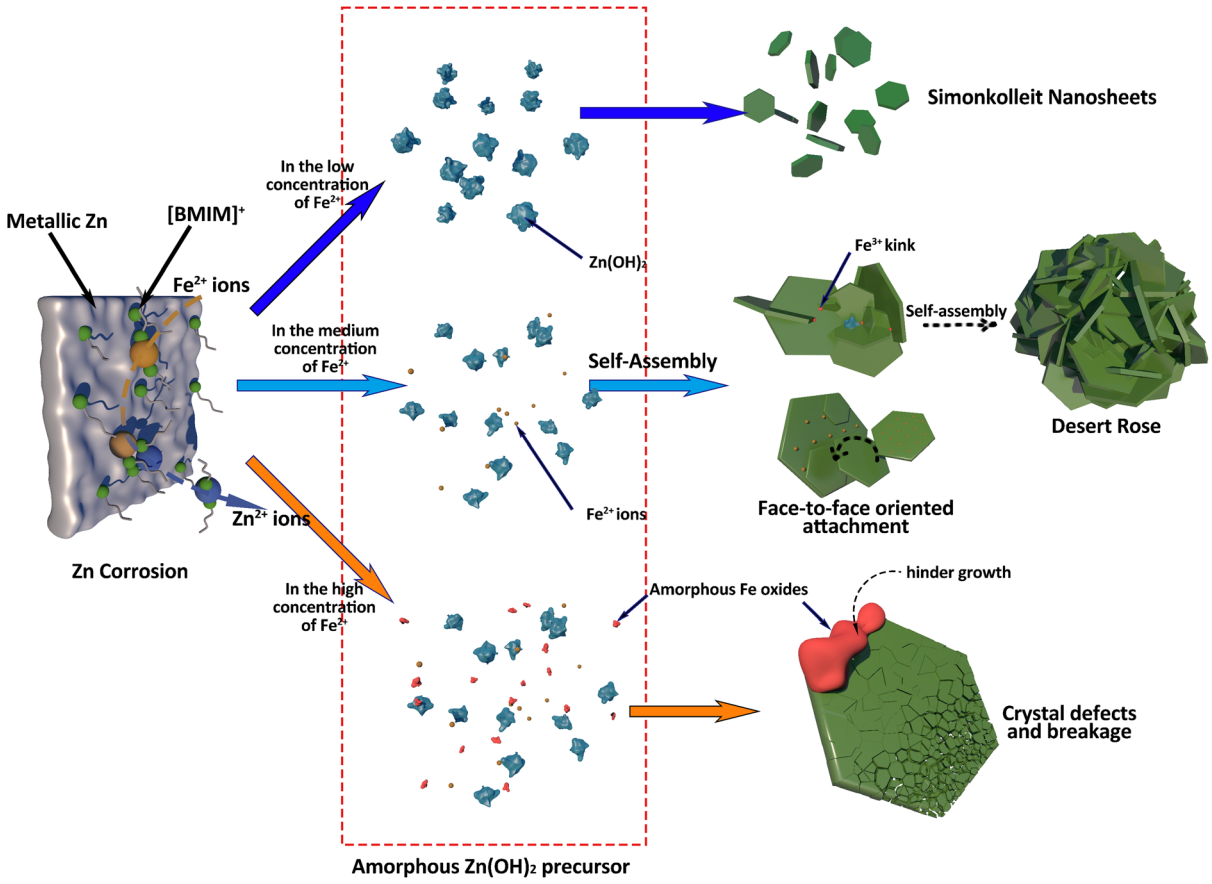

Figure 9. Schematic of Zn-based LDH formation mechanism in [BMIM]Cl with different $FeCl_2$ concentration doping.

The optical properties of LDH photocatalysts with varying $FeCl_2$ doping concentrations were investigated using photoluminescence spectroscopy (PL) and UV–vis diffuse reflectance spectroscopy (DRS). The characteristic emission bands observed in the PL spectra (Figure S8, Supporting Information) are generally associated with the recombination rate of photogenerated charge carriers in photocatalysts.[67] All samples exhibit an emission peak at ≈470 nm, which can be attributed to the band-band PL phenomenon induced by photogenerated charge carriers. With increasing $FeCl_2$ concentration, the PL emission intensity decreases. This quenching effect indicates that the recombination rate of photogenerated charge carriers in the ZnFe-LDH photocatalysts is partially suppressed, thereby promoting the photocatalytic activity of the material.

Figure S9, Supporting Information presents the DRS spectra of ZnFe-LDH composites doped with different concentrations of $FeCl_2$. The results indicate that $FeCl_2$ doping moderately influences the light absorption properties of the ZnFe-LDH composites. All samples exhibit a distinct absorption edge below 400 nm in the UV region, while most light in the visible spectrum is reflected. Increasing the $FeCl_2$ concentration in the composites slightly broadens the absorption edge into the visible light region ($\lambda > 400$ nm), suggesting a moderate enhancement in the photocatalytic activity of the material under visible light irradiation.

The quantum yield for photocatalytic hydrogen production is a measure of the efficiency of the process in converting absorbed photons into the desired chemical product (hydrogen), However, challenges arise in determining absorbed photons or reacted electrons due to issues such as light scattering and reflection. Considering these practical complications, the International Union of Pure and Applied Chemistry (IUPAC) suggests employing the term "apparent quantum yield" (AQY), which is calculated as:[68]

$$\begin{aligned} \mathrm{AQY}(\%) &= \frac{\text{number of reacted electrons}}{\text{number of incident photos}} \times 100\% \\ &= \frac{2R_{H_2}}{I_0} \times 100\% \end{aligned} \tag{14}$$

where R_{H_2} is the apparent rate of hydrogen production. A maximum apparent quantum yield value of 0.51% was obtained at a wavelength of 334 nm in the presence of $FeCl_2$ doping concentrations at 0.45 M.

Zn–Fe LDH (0.36 M) exhibits excellent stability as a photocatalyst for hydrogen production. This is evident by the consistent H_2 evolution activity observed over three consecutive reaction cycles (Figure S4, Supporting Information). Table S3, Supporting Information provides a comparison of the hydrogen production efficiency reported in the literature for different

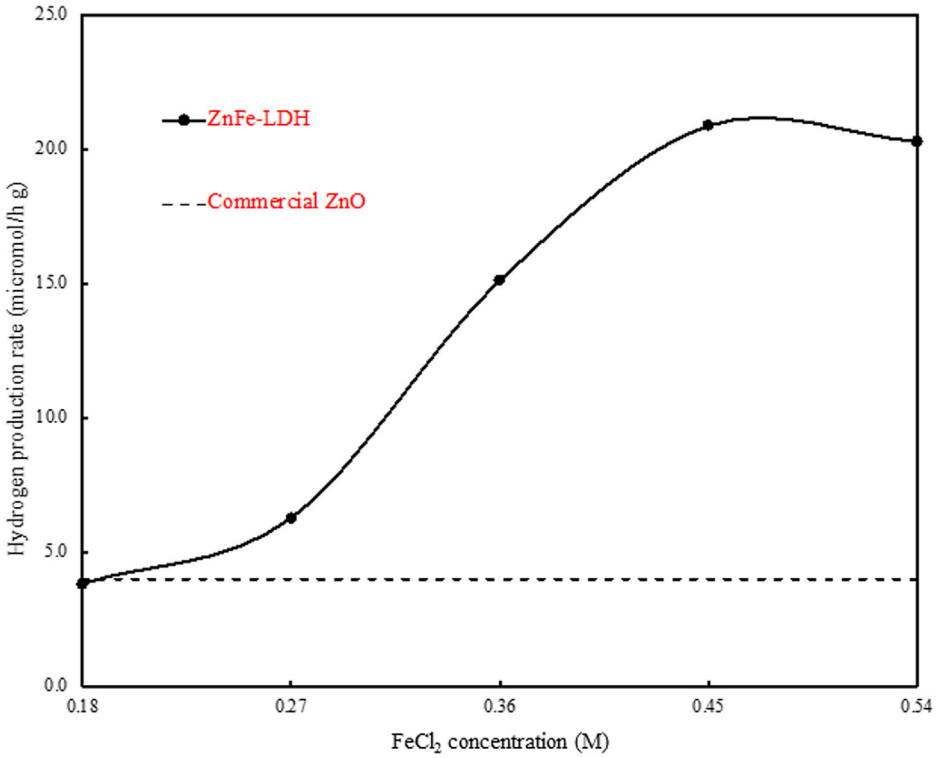

Figure 10. Hydrogen production rate from methanol photoreforming obtained using Zn-based LDH synthesized with different concentrations of $FeCl_2$.

LDH-based photocatalysts. While most LDH-based photocatalysts reported in the literature are typically synthesized through coprecipitation or hydrothermal methods, the photocatalyst presented in this study stands out due to its environmentally friendly synthesis method. Although its hydrogen production rate is not the highest, the synthesis method presented in this work emphasizes sustainability and demonstrates considerable potential. Future work could focus on the incorporation of co-catalysts to further enhance the photocatalytic hydrogen production rate.

3. Conclusion

This work presented the synthesis of a series of Zn-based LDHs using the OIS method and proposed a detailed crystal growth mechanism for Zn-based LDHs. Our investigation examined the composition and crystal morphologies of the products under three doping scenarios: NaCl, $ZnCl_2$, and $FeCl_2$.

The study revealed that doping ions have a significant impact on the oxidation and reprecipitation kinetics of metallic Zn in [BMIM]Cl, with the rate order being $Fe^{2+} > Zn^{2+} > Cl^-$. Notably, the formation of Zn-based LDH occurs only in environments with a relatively high Zn^{2+} concentration (>0.18 M), which can be achieved either by adding extra Zn^{2+} or introducing Fe^{2+} to accelerate Zn corrosion.

This study focuses on the impact of Fe^{2+} ion doping on the crystal morphologies and photocatalytic performance of Zn-based LDH. In Fe^{2+}-doped environments, sufficient Fe^{2+} incorporation into the lattice leads to Zn–Fe(II) LDH formation, resulting in a unique desert-rose-shaped structure due to increased lattice defects and polarity. The synthesized Zn–Fe(II) LDH further oxidizes in air, forming a stable Zn–Fe(III) LDH. However, excessive Fe^{2+} introduces instability, leading to the formation of porous lamellar crystals.

When tested for hydrogen production through photoreforming of methanol, the synthesized Zn–Fe(III) LDH exhibits a hydrogen production rate of 20.9 $\mu mol\, h^{-1}\, g^{-1}$, obtained using a $FeCl_2$ doping concentration of 0.45 M. This corresponds to an AQY of 0.51% (at 334 nm) which is five times higher compared to commercial zinc oxide.

Compared to simonkolleite, the crystal structure of Zn–Fe LDHs is more complex and variable. The bonding interactions between the metal ions and anions remain a subject of debate, and further research is needed to fully elucidate their structure. Additionally, comparative studies exploring the catalytic performance of single LDH materials with controlled morphologies are limited. Developing mixed LDHs using cost-effective and scalable methods to achieve high purity and quality remains a challenge. The complexity of the LDH structure also complicates the investigation of its photocatalytic mechanisms, particularly in hydrogen production from photoreforming.

Supporting Information

Supporting Information is available from the Wiley Online Library or from the author.

Acknowledgements

The authors gratefully acknowledge Ian M Ross and Jiahui Qi at the Sorby Centre for their support and assistance in the use of the electron microscopy facilities of the University of Sheffield. The authors acknowledge Gareth Williams from the School of Mathematical and Physical Sciences of the University of Sheffield, and Pengwei Deng from the East China University of Science and Technology for the support with PL and UV–vis DRS.

Conflict of Interest

The authors declare no conflict of interest.

Author Contributions

Shaoqing Qu: conceptualization (lead); data curation (lead); formal analysis (lead); investigation (lead); methodology (lead); visualization (lead); writing—original draft (lead); writing—review & editing (supporting). **Ruiman Ma**: data curation (supporting); formal analysis (equal); methodology (supporting); writing—original draft (supporting); writing—review & editing (supporting). **Igor Efimov**: data curation (supporting); formal analysis (equal); methodology (equal); software (supporting); writing—original draft (supporting). **Sergio Vernuccio**: data curation (supporting); funding acquisition (equal); methodology (equal); resources (equal); supervision (equal); writing—review & editing (equal). **Eftychios Hadjittofis**: supervision (supporting); writing—review & editing (supporting). **Kyra Sedransk Campbell**: funding acquisition (lead); supervision (lead); writing—review & editing (lead).

Data Availability Statement

The data that support the findings of this study are available from the corresponding author upon reasonable request.

Keywords

ionic liquids, layered double hydroxides, photocatalysis, oxidative ionothermal synthesis, zinc corrosion

Received: September 26, 2024
Revised: December 20, 2024
Published online:

[1] D. Basu, A. Das, K. W. Stöckelhuber, U. Wagenknecht, G. Heinrich, *Prog. Polym. Sci.* **2014**, *39*, 594.
[2] S. A. A. Abdel Aziz, Y. GadelHak, M. B. E. D. Mohamed, R. Mahmoud, *Sci. Rep.* **2023**, *13*, 1.
[3] F. Mohamed, M. R. Abukhadra, M. Shaban, *Sci. Total Environ.* **2018**, *640–641*, 352.
[4] C. B. Ong, L. Y. Ng, A. W. Mohammad, *Renewable Sustainable Energy Rev.* **2018**, *81*, 536.
[5] J. D. Holladay, J. Hu, D. L. King, Y. Wang, *Catal. Today* **2009**, *139*, 244.
[6] P. Shandilya, R. Sharma, R. K. Arya, A. Kumar, D.-V. N. Vo, G. Sharma, *Int. J. Hydrogen Energy* **2022**, *47*, 37438.
[7] X. Bian, S. Zhang, Y. Zhao, R. Shi, T. Zhang, *InfoMat* **2021**, *3*, 719.
[8] A. Sherryna, M. Tahir, W. Nabgan, *Int. J. Hydrogen Energy* **2022**, *47*, 862.
[9] C. G. Silva, Y. Bouizi, V. Fornés, H. García, *J. Am. Chem. Soc.* **2009**, *131*, 13833.
[10] K. Parida, L. Mohapatra, *Dalton Trans.* **2012**, *41*, 1173.
[11] H. Zazoua, A. Boudjemaa, R. Chebout, K. Bachari, *Int. J. Energy Res.* **2014**, *38*, 2010.
[12] K. Parida, M. Satpathy, L. Mohapatra, *J. Mater. Chem.* **2012**, *22*, 7350.
[13] H. Zhao, R. T. Ma, H. T. Zhao, *J. Mater. Eng.* **2018**, *46*, 38.
[14] F. Leroux, M. Adachi-Pagano, M. Intissar, S. Chauvière, C. Forano, J. P. Besse, *J. Mater. Chem.* **2001**, *11*, 105.
[15] G. Mascolo, *Appl. Clay Sci.* **1995**, *10*, 21.
[16] U. Costantino, F. Marmottini, M. Nocchetti, R. Vivani, *J. Inorg. Chem.* **1998**, *1998*, 1439.
[17] F. Malaret, J. Hallett, K. S. Campbell, *Mater. Adv.* **2020**, *1*, 3597.
[18] F. Samari, S. Dorostkar, *J. Iran. Chem. Soc.* **2016**, *13*, 689.
[19] J. Dupont, M. R. Meneghetti, *Curr. Opin. Colloid Interface Sci.* **2013**, *18*, 54.
[20] G. Xinpei, *Design and Evaluation of Functional Zwitterionic Ionic Liquids Self-Assemblies*, Shandong University **2017**, 124.
[21] H. Li, P. S. Bhadury, B. Song, S. Yang, *RSC Adv.* **2012**, *2*, 12525.
[22] S. Qu, E. Hadjittofis, F. Malaret, J. Hallett, R. Smith, K. S. Campbell, *Nanoscale Adv.* **2023**, *5*, 2437.
[23] L. Wang, X. Lu, X. Wei, Z. Jiang, S. Gu, Q. Gao, Y. Huang, *J. Anal. At. Spectrom.* **2012**, *27*, 1667.
[24] M. Mohammadzadeh, H. Bagheri, S. Ghader, *Arabian J. Chem.* **2020**, *13*, 5821.
[25] K. Moffat, *The Novel Ionothermal Synthesis of Zinc Oxide for Cosmetic Application*, Imperial College, London **2019**.
[26] H. Zhu, J. F. Huang, Z. Pan, S. Dai, *Chem. Mater.* **2006**, *18*, 4473.
[27] Y. Jiang, Z. Shen, C. S. Tang, B. Shi, *Sci. Total Environ.* **2023**, *903*, 166245.
[28] J. Kameliya, A. Verma, P. Dutta, C. Arora, S. Vyas, R. S. Varma, *Inorganics* **2023**, *11*, 121.
[29] K. Morimoto, K. Tamura, S. Anraku, T. Sato, M. Suzuki, H. Yamada, *J. Solid State Chem.* **2015**, *228*, 221.
[30] A. Al-Rasheedi, E. Shalaan, A. A. Hassaneen, M. S. Aida, *ChemistrySelect* **2023**, *8*, e202300909.
[31] S. Cousy, N. Gorodylova, L. Svoboda, J. Zelenka, *Chem. Pap.* **2017**, *71*, 2325.
[32] M. Gazitúa, P. Fuentealba, R. Contreras, R. Ormazábal-Toledo, *J. Phys. Chem. B* **2015**, *119*, 13160.
[33] S. T. Handy, M. Okello, D. Bwambok, in *Proc. - Electrochemical Society* **2006**, pp. 548–555.
[34] C. Zhong, T. Sasaki, A. Jimbo-Kobayeshi, E. Fujiwara, A. Kobayashi, M. Tada, Y. Iwasawa, *Bull. Chem. Soc. Jpn.* **2007**, *80*, 2365.
[35] S. A. A. Moaty, A. A. Farghali, R. Khaled, *Mater. Sci. Eng.: C* **2016**, *68*, 184.
[36] S. De Wu, C. Li, S. M. Fang, X. J. Zheng, Z. X. Han, Z. S. Yu, H. X. Wang, R. F. Chen, *J. Synth. Cryst.* **2010**, *39*, 444.
[37] G. Bouboukas, A. Gaunand, H. Renon, *Hydrometallurgy* **1987**, *19*, 25.
[38] S. M. Salaken, E. Farzana, J. Podder, *J. Semicond.* **2013**, *34*, 073003.
[39] C. Pimentel, A. Hernández-Laguna, C. I. Sainz-Díaz, *ACS Earth Space Chem.* **2022**, *6*, 2499.
[40] F. Malaret, *Details on the Interaction of Metals Exposed to Ionic Liquids*, Imperial College, London **2019**.
[41] K. Jacobs, D. Balitsky, P. Armand, P. Papet, *Solid State Sci.* **2010**, *12*, 333.
[42] J. Wang, P. Ma, L. Xiang, *Mater. Lett.*, **2015**, *141*, 118.
[43] S. Liu, K. Zhou, Y. Fang, X. Xu, J. Jiang, X. Guo, W. Zhen, J. Pu, L. Wang, *J. Chin. Soc. Corros. Prot.* **2016**, *36*, 522.
[44] T. Prosek, D. Thierry, C. Taxén, J. Maixner, *Corros. Sci.* **2007**, *49*, 2676.
[45] C. M. Pelicano, M. Donnabelle Balela, *MATEC Web of Conferences* **2015**, *27*, 02007.
[46] Y. Pan, C. Zhao, R. Wang, M. Zhu, W. Zhuang, Q. Li, *Soft Matter* **2024**, *20*, 7420.
[47] W. Zhang, K. Yanagisawa, *Chem. Mater.* **2007**, *19*, 2329.

[48] M. F. Chen, Y. Chen, Z. Jia Lim, M. Wah Wong, *J. Mol. Liq.* **2022**, *367*, 120489.
[49] A. A. Ahmed, Z. A. Talib, M. Z. Hussein, M. H. Flaifel, N. M. Al-Hada, *J. Spectrosc.* **2014**, *2014*, 1.
[50] B. B. V. Salzmann, M. M. Van Der Sluijs, G. Soligno, D. Vanmaekelbergh, *Acc. Chem. Res.* **2021**, *54*, 787.
[51] M. Niederberger, H. Cölfen, *Phys. Chem. Chem. Phys.* **2006**, *8*, 3271.
[52] D. Johannsmann, in *The Quartz Crystal Microbalance in Soft Matter Research: Fundamentals and Modeling*, Springer, Clausthal **2014**.
[53] G. Sauerbrey, *Z. Med. Phys.* **1959**, *155*, 206.
[54] L. Daikhin, E. Gileadi, G. Katz, V. Tsionsky, M. Urbakh, D. Zagidulin, *Anal. Chem.* **2002**, *74*, 554.
[55] M. Volmer, A. Weber, *Z. Phys. Chem* **1926**, *119U*, 277.
[56] V. I. Kalikmanov, in *Nucleation Theory*, Springer, Heidelberg **2013**, pp. 17–41.
[57] H. Li, B. Zhang, W. Jiang, W. Zhu, M. Zhang, C. Wang, J. Pang, H. Li, *Green Energy Environ.* **2019**, *4*, 38.
[58] A. S. Kuz'mina, M. Y. Kuz'mina, M. P. Kuz'min, *Mater. Sci. Forum* **2020**, *989*, 210.
[59] L. Feng, S. Zhang, S. Zheng, Z. Hu, H. Zhu, X. Ma, *J. Chin. Soc. Corr. Prot.* **2022**, *42*, 791.
[60] H. Cao, Y. Hu, W. Xu, Y. Wang, X. Guo, *J. Mol. Liq.* **2020**, *319*, 114354.
[61] H. Kumar, G. Kaur, *Front. Chem.* **2021**, *9*, 1.
[62] S. Vaidya, P. Rastogi, S. Agarwal, S. K. Gupta, T. Ahmad, A. M. Antonelli, K. V. Ramanujachary, S. E. Lofland, A. K. Ganguli, *J. Phys. Chem. C* **2008**, *112*, 12610.
[63] Y. Yin, A. P. Alivisatos, *Nature* **2005**, *437*, 664.
[64] S. Cao, Y. Shang, Y. Liu, J. Wang, Y. Sun, Y. Gong, G. Mo, Z. Li, P. Liu, *Microporous Mesoporous Mater.* **2021**, *315*, 110910.
[65] Y. Suchikova, S. Kovachov, A. Lazarenko, I. Bohdanov, *Appl. Surface Sci. Adv.* **2022**, *12*, 100327.
[66] L. Xu, X. Li, *J. Cryst. Growth* **2010**, *312*, 851.
[67] C. Gao, Y. Li, Z. Zhang, W. Li, J. Zhong, H. Zhang, Y. Zhang, L. Deng, Z. Sun, G. Chen, H. Zhang, L. Wang, C. Zhuang, X. Han, *Chem. Eng. J.* **2022**, *446*, 137301.
[68] S. Cao, L. Piao, X. Chen, *Trends Chem.* **2019**, *2*, 57.